

# Energetics and Propagation of Coronal Mass Ejections in Different Plasma Environments

Jun Lin \*

Harvard-Smithsonian Center for Astrophysics, 60 Garden Street, Cambridge, MA 02138, USA

Received 2002 July 17; accepted 2002 September 9

**Abstract** Based on previous work, we investigate the propagation of CMEs in a more realistic plasma environment than the isothermal atmosphere, and find that it is a slightly faster reconnection for flux ropes to break free. The average Alfvén Mach number  $M_A$  for the inflow into the reconnection site has to be at least 0.013 in order to give a plausible eruption (compared to  $M_A = 0.005$  for the isothermal atmosphere). Taking  $M_A = 0.1$ , we find that the energy output and the electric field induced inside the current sheet match the temporal behavior inferred from the energetic, long duration, CME-associated X-ray events. The results indicate that catastrophic loss of equilibrium in the coronal magnetic field provides the most promising mechanism for major solar eruptions, and that the more energetic the eruption is, the earlier the associated flare peaks. The variation of the output power with the background field strength revealed by our calculations implies the poor correlation between slow CMEs and solar flares. This work also further confirms the explanation we proposed for the peculiar motion of giant X-ray arches and anomalous post-flare loops. Their kinematic pattern and observed heights are determined by the local Alfvén speed and its variation with height.

**Key words:** Sun: CMEs — Sun: atmosphere — Sun: magnetic fields

## 1 INTRODUCTION

Forbes & Priest (1995, hereafter FP) considered a two-dimensional model with a force-free flux rope that loses equilibrium as the photospheric sources of the coronal magnetic field are brought together. When equilibrium is lost, the flux rope jumps to a new equilibrium position at a higher altitude and a vertical current sheet is created below it. The authors pointed out that, in order for this process to produce an eruption, fast reconnection must occur in the current sheet.

How fast should the reconnection be? If there is no limit of any kind to the reconnection rate, the current sheet is quickly dissipated by the reconnection, the flux rope is unrestrained, and smooth escape is guaranteed. However, this means an unnecessarily large inflow Alfvén

---

\* E-mail: [jlin@cfa.harvard.edu](mailto:jlin@cfa.harvard.edu)

Mach number,  $M_A$ , the velocity of the plasma flowing into the reconnection site in units of the local Alfvén velocity,  $V_A$ , and an X-type neutral line appearing in the place of a current sheet. At the other extreme, in the complete absence of reconnection, namely  $M_A = 0$ , the flux rope cannot escape at all. Following the loss of equilibrium, the flux rope oscillates around the position of the upper equilibrium (refer to Forbes & Lin 2000; Lin & Forbes 2000). In the real coronal environment, the dissipation of the current sheet cannot be totally prohibited, so the inflow Alfvén Mach number,  $M_A$ , has to be larger than zero. On the other hand, it is also difficult to imagine that  $M_A$  could be greater than unity since this would lead to the formation of fast-mode shocks in the inflow region of the reconnection site. Thus we can be reasonably certain that  $0 < M_A < 1$  in reality.

The question of how much less than unity  $M_A$  can be yet still leading to a smooth escape has been examined by Lin & Forbes (2000, hereafter LF). They found that if the plasma density of the corona decreases exponentially with height (i.e., isothermal atmosphere), which yields an Alfvén velocity increasing with height at high altitude, then any value of  $M_A > 0.005$  will give a smooth escape. If  $0.005 < M_A < 0.041$ , then the flux rope undergoes some deceleration before it escapes, and once  $M_A > 0.041$ , the flux rope escapes without any deceleration at all. They also found that if the density of the coronal plasma is uniform, which gives an Alfvén velocity decreasing with height, then the flux rope can never escape even if  $M_A$  is as large as unity. This implies that  $M_A$  is just a relative description of the rate of reconnection, and that the basic efficiency of the reconnection is governed by the local Alfvén speed which fundamentally controls the energy conversion at the reconnection site. Because the Alfvén speed is also a function of density, the dynamic behavior of CMEs must depend on the distribution of the plasma in the corona.

In the isothermal atmosphere, magnetic reconnection at a plausible rate, say  $M_A = 0.1$ , can easily produce a robustly energetic eruption with an impulsive acceleration up to  $4000 \text{ m s}^{-2}$  that accelerates the CME from a few  $\text{km s}^{-1}$  to more than  $1500 \text{ km s}^{-1}$  within about 10 minutes (see LF). Correspondingly, the electric field inside the current sheet reaches its maximum of  $4.5 \text{ V cm}^{-1}$  within 10 minutes. An electric field with such an amplitude implies strong heating and particle acceleration, i.e., major flares.

The model of LF also suggests an explanation for the peculiar motion of giant X-ray arches reported by Švestka et al. (1983, 1995, 1996, and 1997) and Švestka & Fárník (1998). The giant X-ray arches are large loops associated with CMEs, similar in form to post-flare loops, but often having a different upward motion: instead of getting continually slower, the arches move upwards at a rate that remains nearly constant or even increases with time. The results of LF showed how the difference can be explained by a reversal of the gradient of the coronal Alfvén speed with height.

In an isothermal atmosphere, the post-flare loops are usually observed at lower altitudes where the Alfvén speed decreases with height, so, the rise rate of the loops should slow down. At higher altitudes where the giant arches usually appear, the Alfvén speed increases with height, and so does the rise rate of the giant arches. The transition between the two different patterns of motion occurs when the reconnection site reaches the altitude where the Alfvén speed of the ambient coronal field starts to increase with height due to the falling off in the coronal density. In this case, the current sheet is dissipated significantly and the giant arches can reach heights up to one and a half solar radii ( $1.5R_\odot$ ) about six hours after take-off.

According to the observations, on the other hand, the predicted altitude that the giant arches (post-flare loops) can reach is too high and the current sheet is dissipated too soon. The

altitudes of giant X-ray arches observed by Švestka et al. (1997) and Švestka & Fárník (1998) are generally less than  $0.6R_{\odot}$  over periods exceeding 24 hours. Ciaravella et al. (2002) reported an event that developed a current sheet that lasted for more than 20 hours. Another event showed an energetic eruption and left behind a current sheet that remained for more than 2 days (Ko et al. 2002). The corresponding EIT data showed apparent growth of the loop system, but the LASCO data (C2) indicated that the height of the lower tip of the current sheet, which is the top of the loop system, never developed beyond the edge of C2, located at the altitude of  $1.3R_{\odot}$  above the limb.

So, the question we need to address here is: what the background field and the coronal density should be in reality in order to yield the “right” Alfvén speed, and thus the “right” reconnection rate, that allows a catastrophic loss of equilibrium in a magnetic system containing a flux rope to produce a plausible CME-like eruption without significantly dissipating the current sheet created by the erupting field? In the present work, we are incorporating changes in the background field and in the distribution of coronal plasma density, so that we are able to look in more detail at the roles played by the background field and the density distribution in the eruptive process, and to better understand any constraints on our eruption models.

In the next section, we look at an empirical atmosphere model developed by Sittler & Guhathakurta (1999, hereafter S&G), and briefly summarize the previous work. In Section 3, we will investigate the impact of the background field and the plasma density distribution on the critical Alfvén Mach numbers. In Section 4, the dynamical behavior of the CME in different coronal environments will be worked out. Section 5 will be an investigation of the upward motions of the loop/giant arches system during a CME/flare, and finally, Section 6 will summarize the present work.

## 2 DENSITY MODELS AND SYNOPSIS OF PREVIOUS WORK

Figure 1 plots the plasma density,  $\rho(y) = \rho_0 f(y)$ , in the corona against the height,  $y$ . Here  $\rho_0 = 1.673 \times 10^{-14} \text{ g cm}^{-3}$ , and  $f(y)$  is a dimensionless function of  $y$ . The height  $y$  is measured from the surface of the Sun and is in units of the solar radius. The dashed line corresponds to a uniform constant density,  $f(y) = 1$ . The dash-dot line is for an isothermal atmosphere with the density decreasing exponentially with the height,  $f(y) = e^{-6.96y}$ . Some features of the dynamical behavior of CMEs in these two atmospheres have been investigated by LF, who illustrated the effect of the density model on the results. These two density distributions actually describe two extreme cases in which the Alfvén speed either goes to infinity at large distance or goes to zero very quickly. So, their results are also extremes in some sense.

The solid curve in Fig. 1 is for an atmosphere of which the  $f(y)$  is given by S&G

$$f(y) = a_1 z^2(y) e^{a_2 z(y)} [1 + a_3 z(y) + a_4 z^2(y) + a_5 z^3(y)], \quad (1)$$

where

$$\begin{aligned} z(y) &= 1/(1+y), & a_1 &= 0.001272, \\ a_2 &= 4.8039, & a_3 &= 0.29696, \\ a_4 &= -7.1743, & a_5 &= 12.321. \end{aligned}$$

This model was developed on the basis of those constructed from *Skylab* white-light coronagraph observations (Guhathakurta et al. 1996) and in situ plasma measurement by *Ulysses* (Phillips et al. 1995). It smoothly connects the density distributions near and far from the Sun. As Fig. 1 shows. The density distribution  $f(y)$  given by Equation (1) describes the isothermal

atmosphere in the lower corona, and then decreases with the distance much more slowly, as  $1/y^2$ . The results of radio observations of type III bursts over a wide waveband from a few kHz to 13.8 MHz also suggest the  $1/y^2$  variation far from the Sun (Leblanc et al. 1998). This means that the atmosphere with density distribution given in Eq. (1) is more realistic than the isothermal atmosphere.

Figure 2 plots the Alfvén velocity profiles corresponding to the above three density profiles. The corresponding profiles are marked with the same type of curves. The background magnetic field of FP is used and the strength of the field at the origin is taken as 100 G. The Alfvén speed decreases to zero at a large distance in the uniform atmosphere, and increases to infinity in the isothermal atmosphere. The scale height of gravitation in the corona is around  $10^5$  km, below which the atmosphere is isothermal. Therefore, the behaviors of the Alfvén speed in the uniform and isothermal atmosphere represent two extremes, and that in the S&G atmosphere is more realistic. We include the former two to help illustrate the effect of the density model on our results. As we shall see, there is significant difference in the long-term evolution in the different atmospheres due to their differing distance dependence of the Alfvén speed.

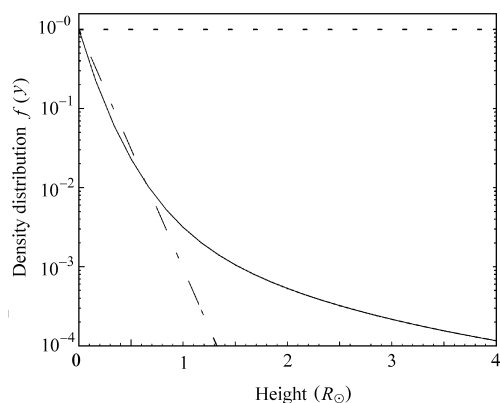


Fig. 1 Plasma density height profiles  $f(y)$ . The dashed line corresponds to the uniform atmosphere with  $f(y) = 1$ , the dash-dot curve is for the isothermal atmosphere with  $f(y) = e^{-6.96y}$ , and the solid curve for the S&G atmosphere with  $f(y)$  given by Equation (1).

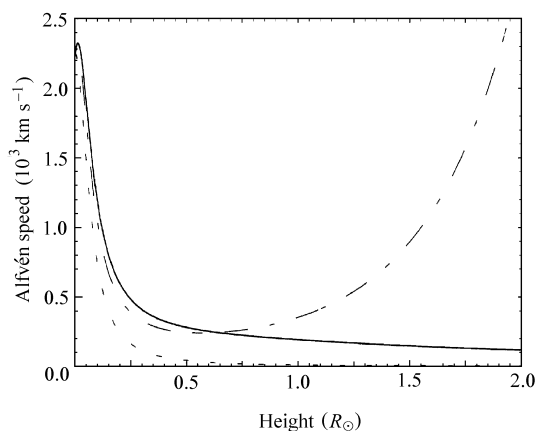


Fig. 2 Variations of the background Alfvén speed as a function of the altitude. Same curve styles as in Fig. 1.

The magnetic field configuration in the system that we are focusing on in the present work is sketched in Fig. 3. At any given time  $t$  a force-free flux rope with radius  $r_0$  is located at height  $h$  on the  $y$ -axis. Below it there may exist a detached, vertical current sheet along the  $y$ -axis with its lower tip at  $y = p$  and upper tip at  $y = q$ . The characteristic values of the main parameters and the basic equations governing the dynamical properties of the system used by LF will again be used in the present work. For illustrative purpose, we list those characteristic values here:

$$\begin{aligned}\lambda_0 &= 5 \times 10^4 \text{ km}, & m &= 2.1 \times 10^6 \text{ g cm}^{-1}, \\ r_{00} &= 0.1\lambda_0, & \rho_0 &= 1.673 \times 10^{-14} \text{ g cm}^{-3}, \\ I_0/c\lambda_0 &= 50\sigma \text{ G}, & \dot{h}_0 &= 1000 \text{ km s}^{-1},\end{aligned}$$

where  $\lambda_0$  is the length scale,  $m$  the mass per unit length inside the flux rope,  $r_{00}$  the initial value of the flux rope radius,  $\rho_0$  the mass density at the base of the corona,  $I_0/c\lambda_0$  is one half the background field strength at the origin,  $I_0$  a constant with dimension of electric current intensity and is also the scale of the intensity of the current inside the flux rope,  $c$  the light speed,  $\sigma$  a dimensionless constant which is taken to be unity by LF, and  $\dot{h}_0$  the velocity scale.

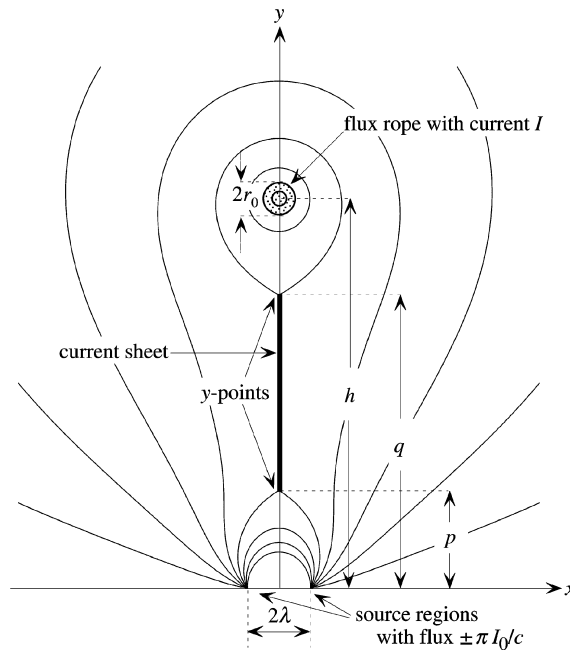


Fig. 3 Diagram of the flux rope configuration showing the mathematical notations used in the text (From LF).

The investigations of FP and LF indicated that the topological properties of the system as well as the evolution of such parameters as the critical point for the catastrophe and the position of the flux rope at the moment a magnetic neutral point appears at the boundary surface, depend neither on the strength of the background field nor on the model of the plasma density. The parameters for the dynamical behavior of the system, on the other hand, do depend on the background strength and the plasma density. For example, the velocity of the flux rope at the moment the current sheet starts to form and the time of this moment are related to the background field strength. The details of the motion of the flux rope following the current sheet formation depend on both the field strength and the distribution of plasma density, and the minimum value of the reconnection rate that allows the flux rope to escape smoothly varies with the form of the density distribution. The separation of two point sources  $\lambda_c$ , the flux rope height  $h_c$ , and the current intensity inside the flux rope  $J_c$  at the critical point,

as well as the values of  $h$  and  $J$  at the moment a neutral point appears at the surface of the Sun,  $h^*$  and  $J^*$ , remain unchanged. These values are (refer to LF)

$$\begin{aligned}\lambda_c &= 0.9695, & h_c &= 1.0966, & J &= J_c = 0.9924, \\ h^* &= 1.8113, & J^* &= 0.9341.\end{aligned}$$

Following the catastrophic loss of equilibrium in the system, the flux rope jumps upward. During the transition of the rope from  $h = h_c$  to  $h = h^*$ , there is still no current sheet. The current sheet starts to develop after  $h > h^*$ . Repeating the relevant calculation in LF, we can obtain for the present case the velocity of the flux rope at the moment the current sheet occurs,  $\dot{h} = \dot{h}^* = 0.3211\sigma$ , and reckoning time from the onset of the catastrophe, we find this moment to be  $t = t^* = 12.21/\sigma$  (min). The consequent dynamical evolution of the system is governed by the following set of ordinary differential equations derived by LF

$$\begin{aligned}\frac{dp}{dt} &= \frac{6}{5}p'\dot{h}, & \frac{dq}{dt} &= \frac{6}{5}q'\dot{h}, \\ \frac{d\dot{h}}{dt} &= \frac{6}{5}\dot{h}'\dot{h}, & \frac{dh}{dt} &= \frac{6}{5}\dot{h}.\end{aligned}\tag{2}$$

Here  $p$  and  $q$  denote the heights of the lower and higher tips of the current sheet, the  $(\prime)$  symbol means taking derivative with respect to  $h$ , and the time  $t$  is in minutes. The expressions for  $p'$ ,  $q'$ , and  $\dot{h}'$  are listed in equation (43) of LF. In order to save space, we shall not reproduce them here, but simply point out the necessary modifications incorporating the changes in the background field and in models of the plasma density in the present work.

Formally, according to the third equation in (43) of LF,  $\dot{h}'$  varies with the background field as  $\sigma^2$ , since it is proportional to  $(I_0/c)^2$ , but it does not explicitly depend on the rate of reconnection or the density profile. In addition, the first two equations in (43) of LF indicate that the reconnection and the density profile affect  $p'$  and  $q'$  via  $\tilde{A}_{0h}$ , which is given by\*

$$\tilde{A}_{0h} = \frac{c}{2I_0} \frac{M_A B_y^2(0, y_0)}{\dot{h} \sqrt{4\pi\rho(y_0)}} + A_{0h},\tag{3}$$

where  $A_{0h}$  was given in equation (28) of LF and no modification is needed in the present work,  $y_0$  is the location of the center of the current sheet, namely  $y_0 = (p + q)/2$ , and the magnetic field  $B_y(0, y_0)$  is given by

$$B_y(0, y_0) = \frac{2I_0}{c\lambda_0} \frac{\lambda(h^2 + \lambda^2)}{(h^2 - y_0^2)(y_0^2 + \lambda^2)} \sqrt{\frac{(y_0^2 - p^2)(q^2 - y_0^2)}{(\lambda^2 + p^2)(\lambda^2 + q^2)}},\tag{4}$$

where  $\lambda$  is fixed at  $\lambda_c = 0.9695$  in our calculation and all other lengths, except  $\lambda_0$ , in this expression are dimensionless. Substituting  $B_y(0, y_0)$  into Eq. (3), and making the necessary normalization, we have [by noticing the fact that  $\rho(y) = \rho_0 f(y)$  with  $\rho_0 = 1.673 \times 10^{-14} \text{ g cm}^{-3}$  and that  $2I_0/c\lambda_0 = 100\sigma \text{ G}$ ]

$$\tilde{A}_{0h} = \frac{2.18M_A\sigma}{\dot{h}\sqrt{f(y_0)}} \left[ \frac{\lambda(h^2 + \lambda^2)}{(h^2 - y_0^2)(y_0^2 + \lambda^2)} \right]^2 \frac{(y_0^2 - p^2)(q^2 - y_0^2)}{(\lambda^2 + p^2)(\lambda^2 + q^2)} + A_{0h}.\tag{5}$$

---

\*Note: the factor  $c/2I_0$  in this equation was missed out in LF.

Solving the coupled equations in Eq.(2) with the  $\tilde{A}_{0h}$  given in Eq.(5) and with the initial condition:

$$\begin{aligned} t &= 12.213/\sigma, \\ h &= 1.8113, \\ \dot{h} &= 0.3211\sigma, \\ p &= 0, \\ q &= 0, \end{aligned} \tag{6}$$

determines the time variations, after the formation of the current sheet, of the flux rope height  $h$ , velocity  $\dot{h}$ , current parameters  $p$  and  $q$ , etc.

The initial conditions Eq.(6) indicate that the stronger the background field is, the earlier the current sheet forms and the earlier the reconnection (thus the flare) occurs. Therefore, how long the flare lags behind the associated CME or eruptive prominence depends on the strength of the background field. This conclusion holds for the cases in which the catastrophe occurs prior to the formation of current sheet. It does not necessarily hold for other cases. For example, in the case that an X-type neutral point or a current sheet appears above the boundary surface before the evolution reaches the critical point for catastrophe (see Forbes & Isenberg 1991; Lin 2001; Lin & van Ballegooijen 2002), energetic reconnection starts almost at the same time as the loss of equilibrium, then the flare and the initiation of the CME or eruptive prominence should be observed simultaneously.

### 3 EFFECT OF BACKGROUND FIELD AND DENSITY PROFILE ON THE CRITICAL ALFVÉN MACH NUMBER

Since there is no generally accepted theory as to how soon the reconnection occurs when it is driven by a loss of equilibrium, we will assume for simplicity that  $M_A$  is a constant less than unity in our calculation (refer to LF for a more detailed discussion on  $M_A$ ). Obviously, if  $M_A = 0$  we are back to the ideal MHD case investigated by FP. In the absence of reconnection and assuming no energy is dissipated, the flux rope oscillates (like a yo-yo) around the upper equilibrium at  $h \approx 8.9$ , and the highest location reached by the flux rope is at  $h \approx 45.1$  (i.e., the height where  $\dot{h} = 0$  and the flux rope starts being pulled back). Our calculation indicates that these two heights are independent of the strength of the background field. This is because they are determined by the competition between the forces of magnetic compression and magnetic tension acting on the flux rope. The magnetic compression is produced by the magnetic field between the boundary surface and the flux rope, and the magnetic tension is due to the field passing over the flux rope, and these two forces depend on the background field in the same way.

In the case of  $M_A > 0$ , escape is possible, but the flux rope may undergo several oscillations before escape occurs as shown by Figs. 4a and 4b, which plot the flux rope height  $h$  as a function of time  $t$  for  $M_A = 0.001$  and  $\sigma = 1$ . Figure 4a is for the isothermal atmosphere model and Fig. 4b for the S&G model with the plasma density distribution given by Eq. (1). In this case, the reconnection is so slow that the flux rope oscillates in nearly the same manner as in the ideal MHD case. However, with each oscillation the rope reaches a greater height because of the ongoing erosion of the current sheet, which weakens the magnetic tension that tends to pull the rope back. In the isothermal atmosphere, the Alfvén velocity increases with height at large

altitudes (Fig. 2), and the erosion of the current sheet at high altitudes speeds up and decreases the magnetic tension so effectively that, on the fourth bounce, the rope breaks free (Fig. 4a). In the S&G atmosphere, on the other hand, the Alfvén speed decreases with height, so the erosion of current sheet at high altitudes is not sufficiently effective as  $M_A$  is too small. Although the flux rope bounces higher and higher on each oscillation (Fig. 4b), there is no apparent sign of escape despite the calculation having been extended over a long time. Even in this case, however, the maximum height reached by the flux rope within the first period of oscillation is large enough ( $> 5R_\odot$ ) for the flux rope to escape, since in a more realistic nonplanar model, the flux rope would be trapped by the solar wind at such a height.

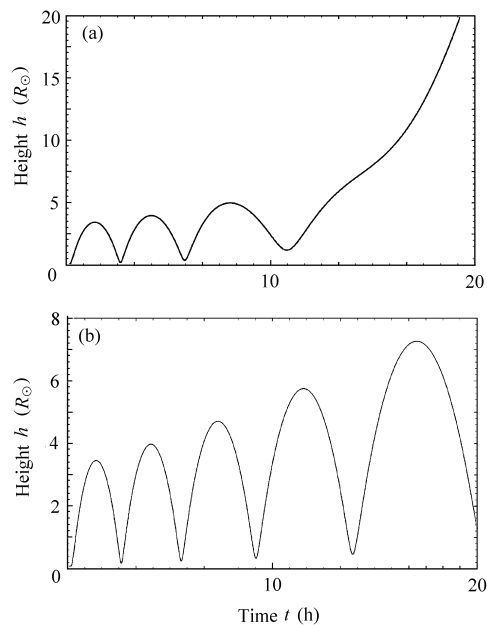


Fig. 4 Time variation of the flux rope height  $h$  for reconnection with  $M_A = 0.001$  in the isothermal atmosphere (a) and in the S&G atmosphere (b). The unrealistic oscillating behavior indicates that this rate of reconnection is too low to give a plausible result.

Wang & Sheeley (2002) identified roughly 20 events that showed fallback characteristics among those observed from 1999 to 2001. These probably are cases represented by Fig. 4. Apparently, compared with the normal CMEs, the fallback events are very rare. To avoid oscillating in the isothermal atmosphere, LF have shown that  $M_A$  must be greater than  $\sim 0.005$ , and that if  $M_A$  exceeds 0.041 the flux rope is able to escape smoothly without undergoing deceleration. For the S&G atmosphere, our calculation in this work shows that  $M_A$  has to be larger than 0.01286 in order to let the flux rope go, and smooth escape takes place when  $M_A \geq 0.03445$ . We notice something interesting here: reconnection in the isothermal atmosphere is more efficient than that in the S&G atmosphere as regards allowing the flux rope to break free, but is less efficient as regards smooth escape without deceleration. The results of LF may help us understand this phenomenon. Acceleration of the flux rope, development of the

current sheet, and the rate of reconnection are coupled with one another. The reconnection dissipates the current sheet and helps the flux rope to escape, the motion of the flux rope in turn helps the current sheet to develop and the associated magnetic tension tends to pull the flux rope back. On the other hand, it is easier for reconnection to take place in a long current sheet due to the plasma instabilities, such as tearing mode instability. Initially, the current sheet forms purely because of the motion of the flux rope caused by the catastrophic loss of equilibrium, which is an ideal MHD process. As the magnetic reconnection becomes significant, development of the current sheet starts to be supported by the flux rope motion that results from erosion of the current sheet itself. So, whether the escape is smooth or not also depends on whether the reconnection can in time erase the part of the current sheet formed as a result of the reconnection itself.

In an isothermal atmosphere, reconnection is so efficient that a fairly small rate of reconnection is able to allow the flux rope to escape. However, the timescale of the reconnection is relatively long, if  $M_A$  is too small to let the erosion of the current sheet catch up with the development, magnetic tension may temporarily dominate over magnetic compression, leading to deceleration. To avoid deceleration, a greater  $M_A$  is required. In the S&G atmosphere, reconnection is not so efficient, so both the motion of flux rope and the development of current sheet are correspondingly slower. The reconnection could have enough time to dissipate a sufficient portion of the current sheet, thus preventing the tension from dominating over the compression, so facilitating a smooth escape.

#### 4 DYNAMICAL PROPERTIES OF CMEs

In addition to the importance of magnetic reconnection for the occurrence of CMEs, we can also investigate their propagation in more detail. The details include the velocity, acceleration, evolution of the current sheet, the energy output, the induced electric field inside the current sheet, as well as the growth of post-flare/CME loop (or giant arch) systems. Solving the differential equations in Eq. (2) under the initial condition Eq. (6) directly determines the flux rope height,  $h$ , velocity,  $\dot{h}$ , acceleration,  $d\dot{h}/dt$ , as well as the current sheet parameters,  $p$  and  $q$ . In LF, the output energy (power),  $P$ , and the induced electric field,  $E_z$ , are then calculated according to

$$P = m\dot{h} \frac{d\dot{h}}{dt}, \quad (7)$$

$$E_z = \frac{M_A B_y^2(0, y_0)}{c\sqrt{4\pi\rho_0 f(y_0)}}, \quad (8)$$

where  $B_y$  is given by Eq. (4). In our previous plots of Figs. 1 and 2, the height  $y$  was in units of the solar radius. In our following calculations, on the other hand, the height  $y$  has to be in units of  $5 \times 10^4$  km in order for us to make use of some existing results of LF. Therefore, the argument  $y$  of the density profile  $f(y)$  must be replaced by  $5y/69.6$ , i.e., we will use  $f(y) = e^{-y/2}$  for the isothermal atmosphere and  $z(y) = 1/(1 + 5y/69.6)$  in Equation (1) for the S&G atmosphere, before we carry out our calculations with Eq. (2).

##### 4.1 Eruption in Isothermal Atmosphere

In this case, the plasma density decreases with height exponentially:  $f(y) = e^{-y/2}$ . Figure 5 plots, for  $M_A = 0.1$ , as functions of the time  $t$ , the flux rope height,  $h$ , velocities  $\dot{h}$ , acceleration

$d\dot{h}/dt$ , the current sheet parameters  $p$  and  $q$ , output power  $P$ , as well as the electric field  $E_z$  inside the current sheet. According to the discussions of LF and Forbes & Lin (2000), the lower tip of the current sheet,  $p$ , is nothing but the top of the post-flare/CME loop (giant arch) system. So, variations of  $p$  also describe the growth of the loop system.

In the panels, the solid curves are for  $\sigma = 1$ , the dashed curves for  $\sigma = 1/2$ , and the dot-dashed curves for  $\sigma = 2$ . The dynamical behaviors in the isothermal atmosphere for  $\sigma = 1$  were studied by LF, and we use the corresponding results here for reference. The overall shapes of the three curves in any one panel are similar for the different values of the magnetic field, but the amplitudes and the temporal scales depend on the field strength. Thus, the strength of the background field,  $\sigma$ , governs the energetics of the eruptive process, but not the manner in which the process evolves. For example, the velocity of the flux rope is proportional to  $\sigma$ , but its evolutionary features are the same for different values of  $\sigma$ ; the amplitude of the acceleration scales as  $\sigma^2$ , its peak time and time scale of evolution scale as  $\sigma$ , but the shape of the curve remains unchanged, etc. This characteristic of CME propagation is further reflected by those bumps in the curves of the output power  $P$ , induced electric field inside the current sheet  $E_z$ , as well as the upper tip of the current sheet  $q$ . The appearance of bumps on these curves results from the overshooting of the flux rope motion in the isothermal atmosphere, which we have discussed shortly before. (We will notice later that the bumps disappear in the S&G atmosphere.)

Because the Alfvén speed increases with height at large altitudes in the isothermal atmosphere, so does the reconnection speed and hence so does the erosion of the current sheet: a long current sheet cannot be sustained over a long time, it quickly shortens after the magnetic reconnection dominates the evolution. Therefore, a fixed maximum exists for the length of the current sheet no matter how strong the background field  $\sigma$  is (Fig. 5h). The background field  $\sigma$  only governs the time when this maximum is reached, and the time interval (in terms of the half width of the curve profile) during which the current sheet remains. This is due to the fact that the development and the erosion of the current sheet depend on  $\sigma$  in the same way.

Since the lower tip  $p$  of current sheet is the top of the post-flare/CME loop system, Figs. 5g and 5h imply that flare loops are capable of reaching very high altitudes up to  $2R_\odot$  or even  $6R_\odot$  (depending on the background field strength) in the eruptive process. However, as we already mentioned in the Introduction that the heights of flare loops generally do not exceed  $0.6R_\odot$ , and the LASCO C2 images of those events that apparently developed a long current sheet indicate that the lower tip of the current sheet is always below the edge of C2 which is  $1.3R_\odot$  above the solar limb (Ko et al. 2002; Ciaravella et al. 2002). The reason for this inconsistency is the assumption that the solar corona is isothermal. In fact, the gravitation scale height of the coronal plasma is of order  $10^5$  km beyond which the corona cannot no longer be considered isothermal. As the above calculation is repeated later for the S&G atmosphere, we will see the inconsistency no longer appearing.

Significant impact of the background field  $\sigma$  on the CME process is seen in the amplitudes of the CME velocity (Fig. 5b), acceleration (Fig. 5c), the output power (Fig. 5d), as well as the induced electric field inside the current sheet (Fig. 5e). For  $\sigma = 2$  (the background field at the origin is 200 G, which is about the average strength of the background field), the eruptive process can accelerate the flux rope from zero to more than  $3000 \text{ km s}^{-1}$  within about 20 min with an acceleration up to more than  $1.5 \times 10^4 \text{ m s}^{-2}$ . Correspondingly, the output power  $P$  peaks at  $4.2 \times 10^{30} \text{ erg s}^{-1}$ , and the electric field  $E_z$  at more than  $16 \text{ V cm}^{-1}$ . These values indicate that a catastrophic loss of equilibrium in the coronal magnetic configuration should be

energetic enough to account for the major eruptions.

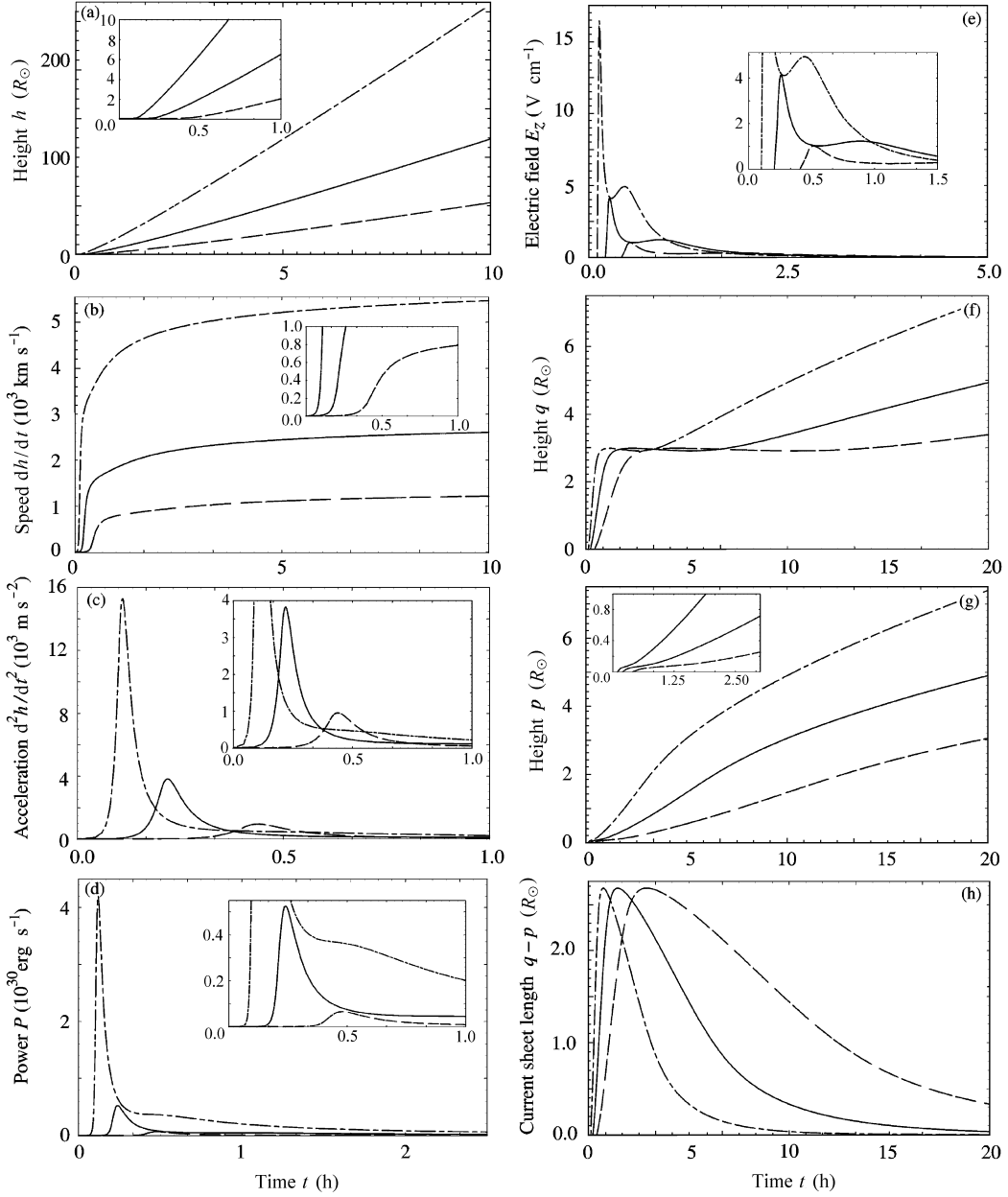


Fig. 5 For the isothermal atmosphere and for  $M_A = 0.1$ : the time variations of the parameters related to the flux rope motion. (a) The height of the flux rope height  $h$ , (b) the velocity  $\dot{h}$ , (c) the accelerations  $\ddot{h}$ , (d) the output power  $P$ , (e) the induced electric field  $E_z$  inside the current sheet, and of the current sheet parameters, (f)  $q$ , (g)  $p$ , and (h)  $q - p$ . Solid, dashed, and dash-dot curves refer to  $\sigma = 1, 0.5, 2$ , respectively. Same units are used for the insets.

On the other hand, we need to point out that our calculation assumes that all the magnetic energy dissipated by the magnetic reconnection is converted into the kinetic energy of the flux rope. In reality, we understand, at least half of the magnetic energy has to go into heating and into the wave energy associated with the generation of a fast-mode shock in front of the flux rope. This implies that the partition of the magnetic energy released may slow down the flux rope from the velocities shown in Fig. 5b by a factor of at least  $\sqrt{2}$ . On the basis of this consideration, it is reasonable to believe that the CME-associated flare peaks at the same time as does the output power  $P$ . So, comparing Figs. 5b and 5d yields that the faster the CME is, the earlier the associated flare peaks. More specifically, this comparison further reveals that for the CMEs with a final velocity greater than  $2000 \text{ km s}^{-1}$  (the above factor of  $\sqrt{2}$  has been counted), the associated flares peak within 15 minutes after the CME onset, and that for those with velocities of around  $1000 \text{ km s}^{-1}$ , the flares peak after about 30 minutes, which somehow has been indicated by the equations in Eq. (6). This result also agrees very well with that of Zhang et al. (2002).

Furthermore, we see from Fig. 5e, for all the three cases of different  $\sigma$  values, the  $E_z$  curve consists of a high peak field followed by a sustained low level field, which is suggestive of the production of the energetic particles inferred from X-rays and  $\gamma$ -rays for large two-ribbon flares associated with CMEs. These flares usually produce a high output of high energy particles, which often account for strong hard X-ray emissions and Type III radio bursts during their impulsive phase, followed by a low level output that is sustained for many hours during the gradual phase (Kanbach et al. 1993).

The correlation between flares and CMEs was first discussed by MacQueen & Fisher (1983) based on the K-coronameter observations, and more recently by Dere et al. (1999), Neupert et al. (2001) and Zhang et al. (2001) based on LASCO observation, and by Alexander et al. (2002) based on both LASCO and Yohkoh observations. Zhang et al. (2001) showed that the early impulsive acceleration phase of CMEs coincides very well with the rise of the associated X-ray flares, and the increase in the CME speed always corresponds to the increase of the soft X-ray flux. The most energetic CME that they observed reached its maximum velocity of  $2000 \text{ km s}^{-1}$  within less than 40 min with an acceleration exceeding  $7000 \text{ m s}^{-2}$ . The CME was accompanied by a flare of importance X9.4 in X-rays and B2 in  $H_\alpha$ .

In addition to working on the LASCO data, Alexander et al. (2002) also analyzed the data from Yohkoh, which helped them to investigate the structure of the CME in soft X-rays and the early stage of the eruptive process. The observations in soft X-rays showed that the ejecta was accelerated up to  $800\text{--}1100 \text{ km s}^{-1}$  within about 500 seconds, and the associated X1.2 flare reached its maximum around 25 minutes after the onset. Applying different fitting profiles to the observational data set, they found that the acceleration was either  $1756 \text{ m s}^{-2}$  or  $4685 \text{ m s}^{-2}$ .

## 4.2 Eruption in S&G Atmosphere

Figure 6 gives plots similar to those in Fig. 5. Except that the coronal plasma density distribution is now given by (1), all the parameters used for Fig. 6 are the same as for Fig. 5. Comparing Figs. 5a, 5b, 5c, 5d, and 5e with Figs. 6a, 6b, 6c, 6d, and 6e suggests that the propagation of CME does not differ greatly in the two environments. The corresponding time profiles have almost the same pattern although the velocity and acceleration are slightly higher in the isothermal atmosphere. An analysis of the peak time of the flare and the velocity amplitude of the associated CME shows the same correlation as that we have discussed shortly before. Because the flux rope in the S&G atmosphere does not overshoot, no bumps appear in

the  $P$ ,  $E_z$ , and  $q$  curves. This makes the curve of output power  $P$  look more like the light-curve of a long-duration events. Comparisons of Figs. 6d and 6e with Figs. 5d and 5e also show that even though the Alfvén speed in the S&G atmosphere decreases with altitude, the eruptions in the S&G atmosphere could be as energetic as those in the isothermal atmosphere, and that the association with flares remains unchanged. The dependence of the output power  $P$  on the background field  $\sigma$  revealed by both Figs. 5d and 6d implies that  $P$  could be fairly low and the associated flare might be too faint to be observed should the CME take place in a configuration with a weak magnetic field.

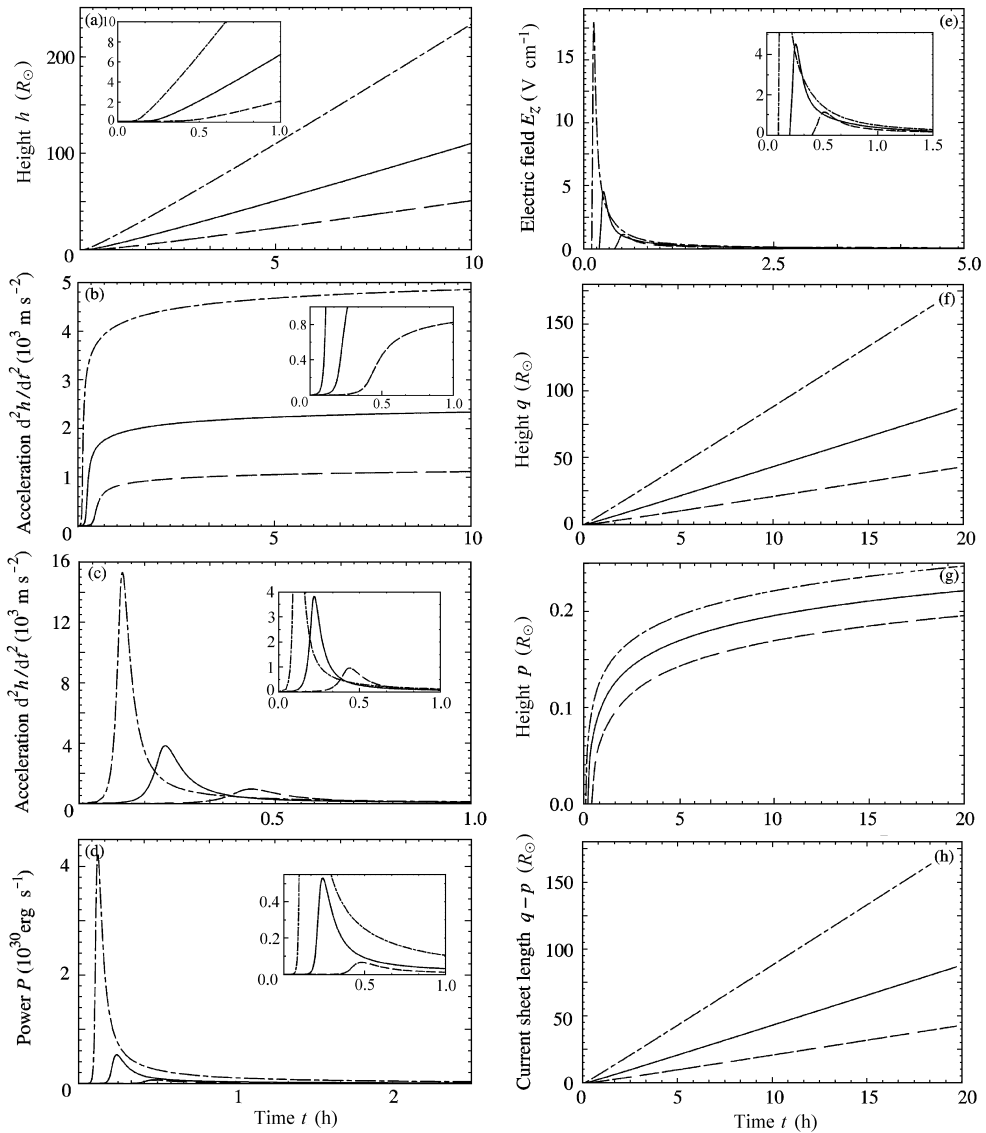


Fig. 6 Plots similar to those in Fig. 5, but for the flux rope motion in the S&G atmosphere.

Comparisons of Figs. 5d and 6d with 5b and 6b further indicate that CMEs occurring in weak magnetic fields are slow and their correlation with flares is poor. Although the validity of the force-free condition applied to our model prevents us from investigating the cases in which the related magnetic field is too weak, the behaviors of  $P$  and  $\dot{h}$  shown by Figs. 5 and 6 are still illustrative and suggestive enough of a continuous variation of the CME-flare correlation with the magnetic field strength. This result is consistent with the argument by Švestka (2001) that there is no difference in principle between slow and fast CMEs, and that the lack of correlation between slow CMEs and flares is because the slow CMEs occur in areas of weak magnetic field. However, Lin & van Ballegooijen (2002) suggested an alternative explanation for the slow CMEs and their poor correlation with flares in which the magnetic field is not required to be weak, and the behavior of the CME depends on the scale of the flux rope as well as on the ambient plasma environment.

The most significant difference in the CME propagation between the two environments, however, comes from the evolutionary behavior of the current sheet. In the S&G atmosphere the local Alfvén velocity keeps on decreasing at large altitudes, so, fast erosion of the current sheet is not expected. As shown by Figs. 6a, 6f, 6g, and 6h, the upper tip  $q$  of the current sheet follows the flux rope and reaches very large heights. It does not manifest any tendency of deceleration. However, the lower tip  $p$  rises quickly during the first one and a half hours after the onset, then keeps on slowing down. The rate of its rise eventually becomes so low that it has only reached  $0.3R_{\odot}$  after more than 20 hours after onset even in the case of  $\sigma = 2$ . The height of  $p$  is even lower in a weak background field. This is suggestive of the fact that the post-flare/CME loop system seldom appears in LASCO images since the top of the loop system is located at  $p$  and the edge of C2 is located at  $1.3R_{\odot}$ . So, we can see a fairly long current sheet that is left behind the CME (Ko et al. 2002; Ciaravella et al. 2002). Further implications of the  $p$  curves in Figs. 5 and 6 will be discussed below.

## 5 UPWARD MOTION OF POST-FLARE/CME LOOPS AND GIANT ARCHES

According to the reconnection models, the upward motion of the lower tip of the current sheet corresponds to the upward motion of either post-flare/CME loops or giant arches. As mentioned in the Introduction, however, the observations indicate that the giant arches typically have a different pattern of motion than the loops. The panels in Fig. 7 demonstrate the difference by comparing the systems of giant X-ray arches and X-ray and  $H_{\alpha}$  post-flare loops of November 6, 1980 (Fig. 7a) and by comparing those of February 21, 1992 (Fig. 7b). The most obvious differences between the two sets of data in each panel are those in the altitudes and lifetimes. The post-flare loops start very close to the surface and then climb either to a height of  $7 \times 10^4$  km over the course of 2 hours (Fig. 7a), or to height of  $1.2 \times 10^5$  km over the course of 12 hours (Fig. 7b). On the other hand, the giant arches start at an altitude of  $7 \times 10^4$  km (Fig. 7a) or  $1.5 \times 10^5$  km (Fig. 7b), and climb to a height of  $1.7 \times 10^5$  km over six hours or to a height of  $2.5 \times 10^5$  km over 18 hours. Apparently, there are overlaps in the altitude at which the loops and giant arches are observed for these two events.

The upward speed of the post-flare loops shows the characteristic pattern of first being rapid at  $15 \text{ km s}^{-1}$  (Fig. 7a) or at  $6 \text{ km s}^{-1}$  (Fig. 7b), and then slowing down with time until the loops are almost stationary at  $1.1 \text{ km s}^{-1}$  (Fig. 7a) or at  $0.3 \text{ km s}^{-1}$  (Fig. 7b) after many hours. By contrast, the giant arches maintain a nearly constant rise of about  $10 \text{ km s}^{-1}$  (Fig. 7a) and a few  $\text{km s}^{-1}$  (Fig. 7b), respectively, with a slight deceleration during the early phase and a

slight acceleration during the later phase (Fig. 7b).

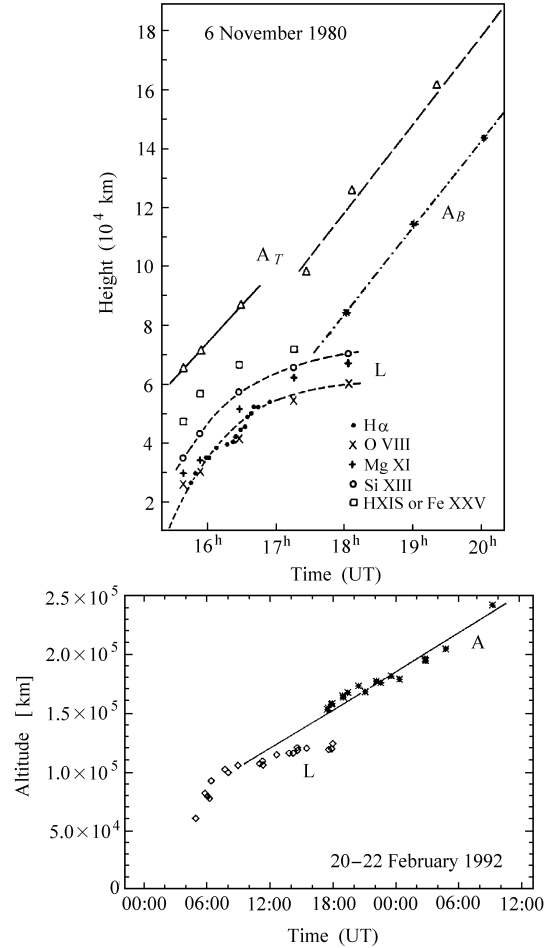


Fig. 7 Comparisons between the trajectories of the giant X-ray arches and the post-flare loops created by flare associated CMEs. (a) Projected altitudes of the post-flare loops (denoted by L) observed both in  $H\alpha$  and by *SMM* instrument, and the rising post-flare giant arches (denoted by either  $A_T$  or  $A_B$ ) observed by HXIS close to the solar limb on November 6, 1980, where  $A_T$  indicates the altitudes of the maximum temperature region of the arch in the fine (solid line) and coarse (dashed line) fields of view of HXIS, and  $A_B$  indicates the altitudes of the maximum brightness of the arch. (b) Altitudes of the maximum brightness region of the arches (denoted by A) and loops (denoted by L) of the flare/CME observed by *Yohkoh* on February 21, 1992. (From Švestka 1996)

Originally, Švestka (1983) proposed that the nearly constant rise rate of the giant arches might mean that they are not produced by reconnection since one would expect their velocity to decrease with height as it does for post-flare loops (see also Simnett & Forbes 1991; Švestka et

al. 1995, 1997). They argued that the upward speed of any loop system created by reconnection should decrease with height since the coronal magnetic field or the Lorentz force that drives the reconnection decreases with altitude, according to Kopp & Pneuman's (1976) model. However, there were also some exceptions that showed the giant arches rising with decreasing speed and the post-flare loop systems rising with constant speed (Švestka 1996). They called those post-flare loop systems anomalous and had a hard time to figure out the physics behind the "anomaly". So, they suggested either that the process proposed by Kopp & Pneuman (1976) for two-ribbon flare was questionable, or there existed two entirely different processes that produce post-flare loop systems, or that the Kopp-Pneuman process creating the post-flare loops at the initial phase of an event had to be substantially modified at the later phase of the loop system development.

As LF and Forbes & Lin (2000) pointed out, however, it is really the Alfvén speed, rather than the magnetic field or the Lorentz force, that is essential for determining the reconnection speed. Because the Alfvén speed is governed by both the local magnetic field and the plasma density, how the reconnection speed varies with the height depends on the combination of the changes in both the magnetic field and plasma density. For example, in our case, both the magnetic field and the plasma density decrease with height in both atmospheres, but the density in the isothermal atmosphere decreases exponentially and faster than does the magnetic field, so, the Alfvén speed increases with height at large altitudes. By contrast, the density in the S&G atmosphere decreases with height exponentially at lower altitudes and then quadratically at higher altitudes, therefore, the effect of the decreasing density on the Alfvén speed is dominated by that of the magnetic field. This leads to an Alfvén speed decreasing with height. Because the Alfvén speed shows different behaviors in different plasma environments, the post-flare/CME loops and giant arches move in different patterns.

As the inset in Fig. 5g shows, the lower tip of the current sheet  $p$ , which is identical with the top of post-flare/CME loop or giant arch system, initially rises at a rapid rate but then starts to slow down with time, before long, it starts to rise rapidly again. The three curves show the same evolutionary pattern, only the time scale of the process is different. So, the motion of  $p$  in the isothermal atmosphere reproduces the evolutionary patterns of both the post-flare loops in the lower corona and the giant arches in the higher corona. Here we are seeing the pattern of the motion of the giant arches and of the "anomalous" post-flare loops. Though their altitudes eventually become unreasonably high as pointed out earlier, it is the patterns of their motion that help us understand the physics behind the observation that bothers us.

On the other hand, as shown by Fig. 6g, after initially rising at a rapid rate, the lower tip of the current sheet  $p$  keeps slowing down and never recovers the rapid motion. The highest altitude  $p$  could reach 20 hours after onset is between  $1.4 \times 10^5$  km and  $3.5 \times 10^5$  km (compared to the altitudes shown in Fig. 5) depending on the strength of the background field. So, in the S&G atmosphere, the motion pattern of  $p$  is that of the post-flare/CME loops but the altitude  $p$  can reach is that of the giant arches. This can be considered as an example of the giant arches that rise with decreasing speed.

Therefore, magnetic field is not the essential factor that definitively determine the kinematic characteristics of the post-flare/CME loops or of the giant arches. Features associated with the lower tip of the current sheet show different patterns of motion because of the different altitude at which they occur relative to the height at which the local Alfvén speed starts to increase or keeps on decreasing, and the magnetic field or the Lorentz force do not directly govern their motion. So, we conclude that the Kopp-Pneuman-type models still work for the eruptions that

manifest giant arches and “anomalous” post-flare loops as long as we understand correctly the roles played by the magnetic field and the local Alfvén speed in the solar eruptive processes.

## 6 CONCLUSIONS

We have investigated the energetics and evolutionary behavior of CMEs in different plasma and magnetic environments. We found that, generally, the magnetic field determines the energetics of the process since it is the magnetic field that provides the energy necessary for driving the process, and that the plasma environment governs the details of the evolution which directly depends on the local Alfvén speed. For the purpose of calculating the time variations we assumed that all of the magnetic energy released goes into the kinetic energy of the flux rope. This obviously overestimates the speed of the flux rope. We understand that, in reality, much (perhaps as much as half) of the energy would be converted into heat and the wave energy associated with the generation of a fast-mode shock in front of the flux rope.

Our more detailed results can be summarized as follows:

1. In the real coronal environment, a modest reconnection rate (as measured by  $M_A$ ) is sufficient to allow the flux rope to break free. The problem of opening up the magnetic field by a purely ideal MHD process first noted by Aly (1984) can be avoided if a reasonable amount of reconnection is invoked following a catastrophic loss of equilibrium.

2. Catastrophic loss of equilibrium in the coronal magnetic configuration followed by magnetic reconnection constitutes the most promising mechanism for energetic eruptions occurring in the solar atmosphere. With a magnetic field of average strength, such a catastrophe can easily produce a major event. If the eruption happens in a weak magnetic field, on the other hand, a slow CME is expected. Because a weak magnetic field may not provide enough energy to drive both CME and flare simultaneously, we can expect a poor association of slow CMEs with flares.

3. A correlation between the peak time of the CME-associated flares to the final velocity of the CME has been deduced. The faster the CME is, the earlier the associated flare reaches its maximum. For CMEs with final velocities greater than  $2000 \text{ km s}^{-1}$ , the associated flare generally peaks within 15 minutes after the onset of the CME; and for those with final velocities around  $1000 \text{ km s}^{-1}$ , the time lag is about 30 minutes.

4. The evolution of the current sheet produced by a CME is determined by the rate of reconnection, which depends on the coronal Alfvén speed. Therefore, by observing the length and height of the current sheet, it is possible to probe the functional behavior of the Alfvén speed in the corona.

5. Both post-flare/CME loops and giant arches are produced by the magnetic reconnection in the Kopp-Pneuman-type process. Their kinematic patterns and the heights where they are observed are not directly related to the magnetic field or the Lorentz force, instead, they are governed by the coronal Alfvén speed and its altitude dependence. This explains why the rise of post-flare loops decelerates and that of giant arches stays constant.

**Acknowledgements** The author is grateful to J. C. Raymond and Z. Švestka for their very helpful and valuable comments and suggestions. This work was supported by NASA grants NAG5-11420 to the Smithsonian Astrophysical Observatory.

## References

- Alexander D., Metcalf T. R., Nitta N. V., 2002, *Geophys. Res. Lett.*, 29, in press
- Aly J. J., 1984, *ApJ*, 283, 349
- Ciaravella A., Raymond J. C., Li J., Reiaer P., Gardner L. D., Ko Y.-K., Fineschi S., 2002, *ApJ*, 575, 1116
- Dere K. P., Brueckner G. E., Howard R. A., Michels D. J., 1999, *ApJ*, 516, 474
- Forbes T. G., Isenberg, P. A., 1991, *ApJ*, 373, 294
- Forbes T. G., Lin J., 2000, *Journal of Atmospheric & Solar Terrestrial Physics*, 62, 1499
- Forbes T. G., and Priest E. R., 1995, *ApJ*, 446, 377
- Guhathakurta M., Holzer T. E., MacQueen, R. M., 1996, *ApJ*, 458, 817
- Kanbach G., Bertsch D. L., Fichtel C. E., Hartman R. C., Hunter S. D., Kniffen D. A., Kwok P. W., Lin Y. C., Mattox J. R., Mayer-Hasselwander H. A., 1993, *A&AS*, 97, 349
- Ko Y., Raymond J. C., Lin J., Lawrence G., Li J., Fludra A. 2002, American Geophysical Union, Spring Meeting 2002, abstract SH21B-07
- Kopp R. A., Pneuman G. W., 1976, *Solar Phys.*, 50, 85
- Leblanc Y., Dulk G. A., Bougeret J.-L., 1998, *Solar Phys.*, 183, 165
- Lin J., 2001, Ph.D. thesis, Physics Dept., Univ. of N. H., Durham, NH, USA
- Lin J., Forbes T. G., 2000, *J. Geophys. Res.*, 105 (No. A2), 2375
- Lin J., van Ballegooijen A. A., 2002, *ApJ*, 576, 485
- MacQueen R. M., Fisher R. R., 1983, *Solar Phys.*, 89, 89
- Neupert W. M., Thompson B. J., Gurman J. B., Plunkett B. J., 2001, *J. Geophys. Res.*, 106 (No. A11), 25215
- Phillips J. L., Goldstein B. E., Gosling J. T., Hammond C. M., Hoeksema J. T., McComas D. J., 1995, *Geophys. Res. Lett.*, 22(23), 3305
- Simnett G. M., Forbes T. G., 1991, In: B. Schmieder and E. R. Priest, eds., *Dynamics of Solar Flares*, Proceedings of the Flare 22 Workshop Held in Chantilly, France October 16-19 1990, L'Observatoire de Paris, Paris, p.121
- Sittler E. C., Guhathakurta M., 1999, *ApJ*, 523, 812
- Švestka Z., 1983, *Space Sci. Rev.*, 35, 259
- Švestka Z., 1996, *Solar Phys.*, 169, 403
- Švestka Z., 2001, *Space Sci. Rev.*, 95, 135
- Švestka Z., Fárník F., 1998, In: T. Watanabe, T. Kosugi, and A. C. Sterling, eds., *Observational Plasma Astrophysics: Five Years of Yohkoh and Beyond*, p. 365
- Švestka Z., Fárník F., Hudson H. S., Uchida Y., Hick P., and Lemen J. R., 1995, *Solar Phys.*, 161, 331
- Švestka Z., Fárník F., Hick P., Hudson H. S., and Uchida Y., 1997, *Solar Phys.*, 176, 355
- Wang Y.-M., Sheeley N. R., Jr., 2002, *ApJ*, 567, 1211
- Zhang J., Dere K. P., Howard R. A., Kundu M. R., White S. M., 2001, *ApJ*, 559, 452
- Zhang M., Golub L., DeLuca E., Burkepile J., 2002, *ApJ*, 574, L97